Electrochemiluminescence (ECL)-based Electrochemical Imaging using a Massive Array of Bipolar Ultramicroelectrodes

Todd J. Anderson,[‡] Peter A. Defnet, [‡] and Bo Zhang*
Department of Chemistry, University of Washington, Seattle Washington 98195 United States

[‡] These authors contributed equally to this work

Corresponding author, zhangb@uw.edu
Phone: 206 543 1767
Fax: 206 685 8665

Abstract. In this report, we describe the fabrication, characterization, and use of a massive array of closed bipolar ultramicroelectrodes (UMEs) in electrochemical imaging applications. The bipolar UME array is 1 cm^2 in size and contains >146,000 carbon electrodes embedded in a 15 μm thick insulating and freestanding membrane of Parylene C. Structural characterization with optical and electron microscopies shows that the carbon UMEs are highly uniform in size, shape, and interelectrode spacing. The bipolar UME array was used in electrochemical imaging to probe highly dynamic redox processes in which the reduction of redox molecules on one side the array is electrically coupled an oxidative electrochemilumescence (ECL) process on the opposite side. This allows one to simultaneously monitor electrochemical reactions on hundreds of thousands of individual electrodes with millisecond temporal resolution. Our results suggest that microfabricated closed bipolar UME arrays can be useful for imaging fast and transient electrochemical processes in which scanning probe methods are inapplicable due to their limited temporal resolution.

Introduction

Electroanalytical methods for imaging redox molecules with high spatial and temporal resolution have sparked significant interest in fields ranging from bioanalysis[1,2] to electrocatalysis.[3-5] In general, these techniques may be classified into two broad groups: scanning probe methods and dual optical-electrochemical imaging. Notable techniques in the former category include scanning electrochemical microscopy (SECM),[6] scanning electrochemical cell microscopy (SECCM),[7] and scanning ion conductance microscopy (SICM).[8] Each of these methods is performed by rapidly scanning a miniscule probe such as an ultramicroelectrode (UME) or quartz nanopipette over a surface of interest while collecting the tip current to map the electrochemical activity and topography of the substrate. While they all can achieve nanoscale spatial resolution,[9] the time required to raster the probe across the sample surface limits their utility in highly dynamic electrochemical systems. In contrast, dual optical-electrochemical methods provide a means of monitoring spatially segregated redox processes at an enhanced temporal resolution. They may also enable the detection of single molecules due to the high sensitivity of optical-based detection.[10,11]

Electrochemiluminescence (ECL)[12] and fluorogenic reactions[13,14] have been employed as probes for direct mapping of electrocatalytic activity; luminol-based ECL systems are also commonly used in hydrogen peroxide sensors.[15,16] However, the processes which may be studied by such direct imaging methods are limited to a few reactions which produce a luminescent product. Changes in the fluorescence of pH-sensitive reporter species have also been utilized to image reactions which alter solution pH,[17-19] but the range of applications for this approach is similarly constrained. The Chen group recently used a fluorogenic reporter reaction to monitor a non-fluorogenic reaction via a competition mechanism.[20] Despite its elegance, this approach may be confined to the study of inner sphere redox species since it relies upon competition between two parallel adsorption processes.

The use of an array of bipolar electrodes (BPEs) to couple an analyte reaction to a complementary reporter reaction provides a more flexible imaging approach. In an open BPE scheme, a driving voltage is used to induce a potential gradient along the surface of a floating electrode. Once the potential difference

exceeds the difference in formal potential of two redox species in the same solution, two half reactions will be coupled to one another on the BPE. If one of these generates an optical signal, such as ECL or fluorescence, one can use the optical response to monitor the reaction on the opposite pole.[21-25] However, due to the competing ionic current pathway in an open BPE system, large electrodes or high driving potentials are often needed to achieve the desired coupling.

Closed BPEs provide an interesting alternative since the parallel ionic current pathway is not present.[26,27] The majority of the applied potential drops across the closed BPE itself, thereby eliminating the need for large electrodes and high driving voltages. An array of closed BPEs can then be used as an electrochemical imaging platform to monitor dynamic changes in redox concentrations. Indeed, our group has previously introduced the fluorescence-enabled electrochemical microscopy (FEEM) in which a fluorogenic reaction was used to image redox processes on an array of carbon fibers.[28-30] While the carbon fibers arrays are easy to prepare, they exhibited poor uniformity and crosstalk due to aggregation of the constituent fibers.[28] The fluorescent reporting species was also prone to fast diffusion, thereby further inhibiting the spatial resolution.

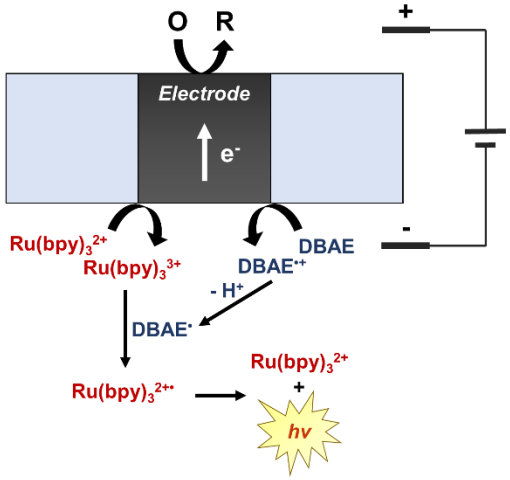

Scheme 1. Diagram of a reduction reaction coupled to a $Ru(bpy)_3^{2+}$-based ECL system with a 2-(dibutyl)aminoethanol (DBAE) co-reactant across a closed bipolar electrode.

Here we present the use of a very large array of microfabricated closed BPEs for imaging highly dynamic redox processes. This flexible BPE array is 1×1 cm^2 in size and is comprised of 146,522 8µm-diameter carbon UMEs arranged in an ordered hexagonal lattice pattern with a 28 µm electrode spacing.

Our BPE array can be prepared with conventional microfabrication tools and has an electrode count over twice that of any individually addressable electrode array reported in the literature.[31-35] Using ECL as the reporter process (see **Scheme 1**), the electrochemical signal can be optically recorded from all of the electrodes with a temporal resolution better than 30 ms. The use of ECL also improves the spatial resolution compared to a fluorescence-based scheme due to the absence of unhindered diffusion of the reporter species. To our knowledge, this is the first instance of ECL-based electrochemical imaging on very large, uniform BPE arrays; other array-based studies have reported a similar detection strategy, but either do not focus on spatially resolving the source of the ECL signal[36-39] or are limited to a spatial resolution of ~0.5 mm.[40]

Experimental Section

Array Fabrication. A Si wafer (Silicon Valley Microelectronics) was cleaned by O_2 plasma (Glow Research) for 5 min (175 W, 1 torr) and spin-coated with SU-8 2050 (MicroChem) photoresist (PR) to yield a 40 μm thick film. The PR film was baked at 65 °C for 3 min and 95 °C for 6 min followed by selective exposure on a mask aligner (ABM-USA). The exposed wafer was then subjected to stress reduction (1 min at 65 °C) and post-exposure baking (6 min at 95 °C). The PR film was then developed in SU-8 developer (MicroChem) for 5 min and rinsed with developer, isopropanol, and DI water before being spun dry.

The SU-8-patterned wafer was diced into ~2×2 cm^2 chips and hard baked in a tube furnace (Thermo Scientific) for 40 min at 300 °C under N_2 flow, after which the temperature was increased to 900 °C for 1 h. The furnace was left closed until it had returned to room temperature. Following pyrolysis, 20 μm of Parylene C was deposited over the patterned chips with a Labcoter 2 system (Specialty Coating Systems) at 175 °C and 690 °C for the vaporizer and pyrolysis furnaces, respectively, and a chamber pressure of 35 mtorr. The Parylene C films were annealed for 2 h at 400 °C under N_2. A PlasmaLab 100 ICP etcher (Oxford Instruments) was used to expose the pyrolyzed carbon structures through the

overlying Parylene. The processed Parylene films were released from Si by overnight immersion in 1 M KOH at 100 °C.

Array Preparation for Imaging. A plastic well was epoxied to the array surface for containment of the top analyte solution. The well was prepared by cutting a 15 mm section from the wide end of a 1 mL pipette tip and attaching it to the array. The ECL solution below the array was contained on the microscope stage using a home-built device fabricated from three 1.0 mm thick glass slides (VWR). One slide was used as the base and two were positioned laterally about 1 cm apart, creating a 1 mm deep channel for ECL solution containment. Epoxy was used to prevent solution leakage.

Bipolar Imaging. Potential was driven across the array using a 3-electrode CV-27 potentiostat (BAS) with three Ag/AgCl electrodes. Two electrodes were placed in the bottom ECL solution, and one was placed in the top solution. Wires were freshly chlorided prior to each experiment using a 1:1 solution of 70% HNO_3 and 3 M KCl. The ECL-CV and redox puffing experiments were recorded on an Andor iXon 897E EMCCD camera cooled to -80 ºC with 30 ms exposure, 300 EM Gain, 5.1x pre-amplifier gain, 0.3 µs vertical pixel shift speed, and 10 MHz readout rate. Videos contained 1500 frames with 512×512 pixels. An Olympus IX70 microscope equipped with a 4x (0.1 NA Olympus Plan N) objective was used to image the array. Each pixel measured 3.92 µm, yielding a 4.0×10^6 μm^2 field of view and allowing 6005 full electrodes in each frame.

The generator-collector and depletion zone imaging experiments were recorded using an Andor Luca S 658M EMCCD cooled to -20 ºC with 30 ms exposure; 0.6 µs vertical pixel shift speed, and 13.5 MHz readout rate. Videos contained 1500 frames with 658×496 pixels. The same IX70 microscope and 4x objective were used. Each pixel measured 1.03 µm, yielding a 3.5×10^5 μm^2 field of view and allowing 507 full electrodes to be viewed in each frame. All videos were analyzed using ImageJ.

An optically-correlated bipolar CV was driven between 100 mM $Fe(CN)_6^{3-}$ 100 mM KCl solution on top of the array, and 25 mM $Ru(bpy)_3^{2+}$ 20 mM DBAE 100 mM phosphate buffer (PB) pH 7.4 below the array. Potential was scanned from 0 to +2.8 V to 0 V vs. Ag/AgCl at 200 mV/s using a CV-27

potentiostat. The current-potential (*i*-*V*) trace was recorded using a LabVIEW 2013 program, while the ECL intensity-potential (I_{ECL}-*V*) trace was simultaneously monitored using conditions described above.

In the generator-collector experiment, a 12.7 μm diameter Au UME was positioned using a Sutter MP-225 micromanipulator in 50 mM $Fe(CN)_6^{4-}$ 1 M KCl solution ~100 μm above the array surface. A 0.8 V potential was applied on the Au UME vs. Ag/AgCl to generate $Fe(CN)_6^{3-}$ at the electrode surface. The $Fe(CN)_6^{3-}$ then diffused to the array surface, which was biased at +2.0 V, and underwent electrochemical reduction by coupling to anodic ECL across each closed-bipolar electrode. The solution used in the ECL experiment was 5 mM $Ru(bpy)_3^{2+}$ 20 mM DBAE 100 mM PB pH 7.4.

To image the depletion zone, a similar procedure was followed as for the above generator-collector experiment. Important differences include the use of a 50 μm Au UME as the generator electrode and maintaining a stationary electrode position throughout the experiment. The Au electrodes for both experiments were fabricated by sealing a piece of Au wire in a glass capillary.[41] Electrodes were characterized using cyclic voltammetry in 1 mM FcMeOH 100 mM KCl solution.

For the redox concentration mapping experiment, a pulled glass micropipette[42] with a 10 μm orifice was immersed in 100 mM KCl solution and was used to inject 100 mM $Fe(CN)_6^{3-}$ 100 mM KCl solution orthogonally onto the array surface. An Eppendorf Femtojet was used to apply constant injection pressures for a controlled period ranging from 1 to 10 s with pressures ranging from 0.5 to 2 PSI. The micropipette was placed ~100 μm above the array surface and remained at a constant distance for the duration of the experiment. Following each stimulation, $Fe(CN)_6^{3-}$ was reduced across the array surface, which was coupled to an anodic ECL process to generate an optical output. A 2.8 V potential was applied across the array to drive the bipolar reaction. The solution used in the ECL experiment consisted of 25 mM $Ru(bpy)_3^{2+}$ 20 mM DBAE 100 mM PB at pH 7.4.

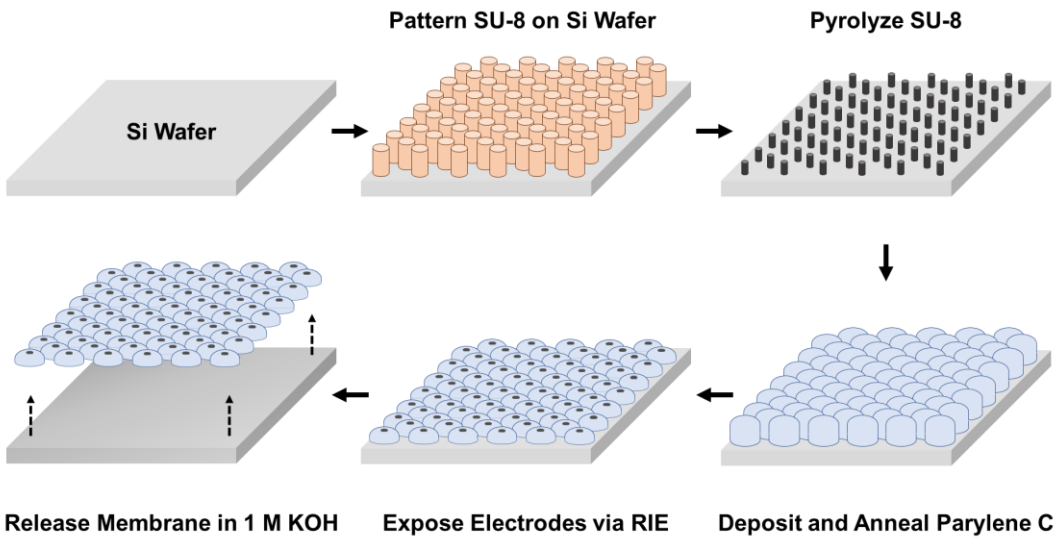

Figure 1. Flowchart illustrating each step of the bipolar UME array fabrication process.

Results and Discussion

Fabrication of Bipolar UME Arrays. A bottom-up process was developed to fabricate the BPE arrays. As summarized in **Figure 1**, our method involves making a large, uniform array of carbon UMEs on a Si substrate, insulating it in a thin Parylene film, and exfoliating the array from the substrate. Several key factors need to be considered. First, since the array resolution is limited by the electrode size and spacing, closely spaced UMEs are desirable to attain maximum density. The insulating film must also be robust and continuous to prevent passage of ionic current. Lastly, the device must be as thin as possible to minimize electrical discontinuities which could arise from high aspect ratio electrode geometries.

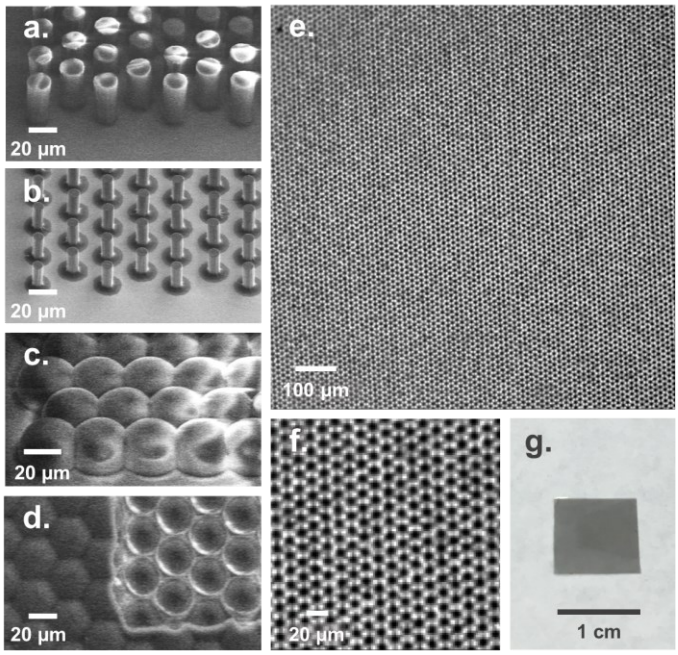

Figure 2: (a) SEM images of SU-8 micropillars (18 µm diameter, 40 µm height) on Si, (b) pyrolytic carbon micropillars (8 µm diameter, 18 µm height), (c) carbon micropillars coated in a 20 µm Parylene C film, (d) a portion of the pyrolytic carbon micropillars exposed. (e) Brightfield optical micrograph of the reporting surface of the array. (f) Close-up view of the array surface. (g) Photograph of a freestanding bipolar UME array.

We adapted a procedure from Wang, *et al.*[43] to generate large arrays of carbon micropillars. A high-temperature pyrolysis process turns an array of SU-8 micropillars into an array of conductive carbon posts. Note from **Figures 2a** and **2b**, however, that the height and diameter of each micropillar is reduced by a factor of two during pyrolysis. This volume loss plays a role in determining the final device thickness and must be considered by selecting an SU-8 thickness twice that of the desired micropillar height.

The carbon array was insulated by Parylene C, a flexible coating widely used in the electronics industry[44-46] due to its excellent electrical properties and chemical resistance. A continuous film may be formed about the carbon micropillars once sufficient growth has occurred on their sidewalls (**Figure 2c**). With this in mind, the SU-8 precursor structures were hexagonally arranged to minimize both the edge-to-edge electrode spacing and, by extension, the thickness of Parylene C required to form a continuous film.

The use of a hexagonal lattice arrangement also resulted in a 15% increase in electrode density compared to a square lattice.

We used thermal annealing to prevent stress fractures in the free-standing membranes after exfoliation. This annealing process increases the tensile strength and elongation-at-break of the Parylene film. Melting and reflowing of the Parylene also renders the substance amorphous and serves to seal any unfilled voids which would result in the passage of ionic current through the insulating layer during device operation. We used O_2 plasma etching to expose the upper carbon surfaces (**Figure 2d**). A hot KOH solution was used to dissolve the Si and free the devices. No degradation or etching of the Parylene or electrodes was observed. Note the uniformity of the electrodes and absence of defects shown in **Figures 2e** and **2f**. A finished device is pictured in **Figure 2g**.

Electrochemical Imaging. Electrochemical imaging experiments were performed to characterize the array's response dynamics, as well as to explore a previously unreported imaging application. Four unique experiments are described along with their independent analyses. We quantify the homogeneity of the ECL response across each array electrode, provide proof for the absence of cross talk, demonstrate the capacity to image variable redox concentrations, and explore the generation of depletion zones in confined spaces using a generator-collector apparatus. Overall, we aim to highlight the excellent performance and broad applicability of our newly fabricated closed-bipolar array for electrochemical imaging.

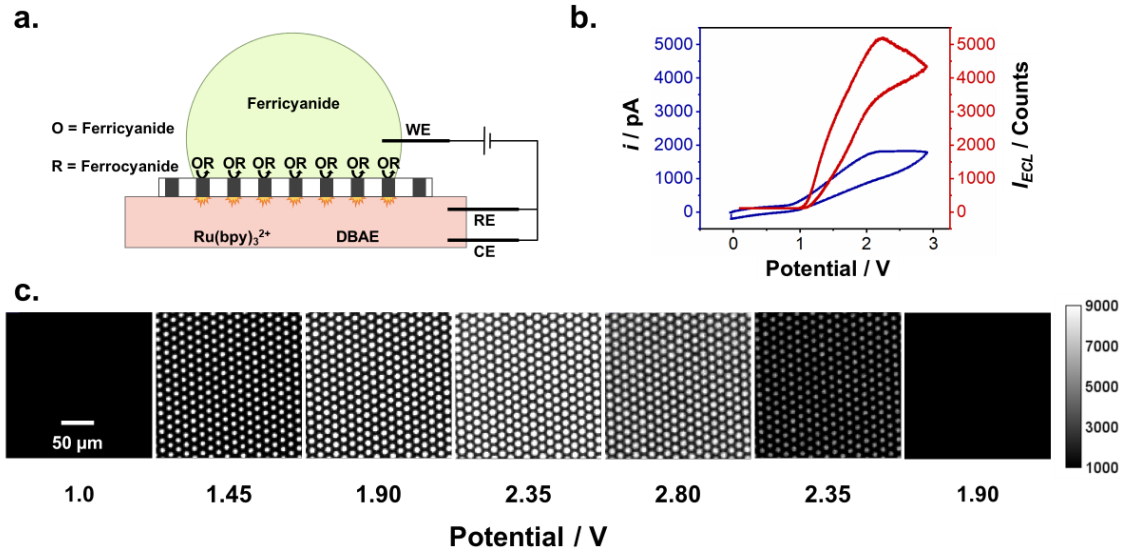

Figure 3. (a) Schematic of an ECL-CV coupling 100 mM $Fe(CN)_6^{3-}$ to anodic ECL across the bipolar array. Potential was swept from 0 to 2.8 to 0 V at 200 mV/s. (b) Correlation of the electrochemical (*i-V*) and optical (I_{ECL}-*V*) signals. The *i-V* signal is representative of the whole array, while the optical signal was averaged across a ~300 electrode subset, including the inactive substrate between electrodes. (c) ECL response from a ~300 electrode subset demonstrating the homogeneity of the I_{ECL} at each electrode for the described potentials. A full video of this process is shown in **Movie S1**.

We first investigated the homogeneity of the ECL intensity (I_{ECL}) on the array by performing a correlated ECL-cyclic voltammogram (ECL-CV). Here, bulk 100 mM $Fe(CN)_6^{3-}$ is placed on top of the array and coupled to anodic ECL solution below the array by reversibly scanning the potential from 0 to 2.8 V, as shown in **Figure 3a**. Both electrochemical (*i-V*) and optical (I_{ECL}-*V*) voltammograms were plotted in **Figure 3b**. The two signals match well in their overall shape, where both onset potentials begin at ~1.1 V and approach a maximum value at ~2.1 V. Interestingly, the I_{ECL} begins to decrease despite increasing potential at 2.3 V, possibly due to interference from other redox reactions such as water oxidation.

The optical response of a ~300-electrode subset of the array during the potential scan is displayed in **Figure 3c** to show single electrode responses. We observe that the I_{ECL} at each electrode is indeed uniform relative to its adjacent electrodes. We aimed to further quantify this homogeneity by plotting

each individual electrode's I_{ECL} response at correlated potentials, as shown in **Figure S1a**. The plotted results demonstrate that the ECL intensity changes uniformly with scanned potential across the array subset. In **Figure S1b** we expand the analysis of individual electrode I_{ECL}-values across all 6000 non-edge electrodes within the recorded field of view. Much variability is observed between the I_{ECL} for electrodes within this large region as evidenced by the wide distribution at each potential. However, examination of a single frame during the scan in **Figure S1d** allows us to conclude that the variation is present only in the upper left and lower left corners of the array, likely due to those regions extending slightly below the focal plane of the microscope objective. Since the 300-electrode subset is entirely within the same focal plane, it will be treated as the metric for comparison. We therefore conclude that the I_{ECL} response is indeed identical across equivalent electrodes.

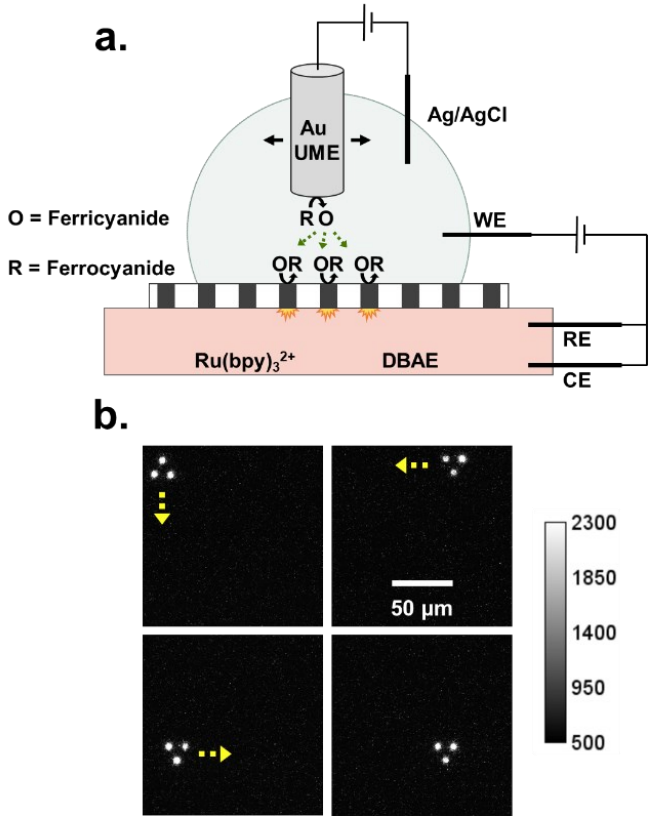

Figure 4. (a) Schematic showing the anodic ECL detection of a diffusion layer on an UME. $Fe(CN)_6^{4-}$ is oxidized on a 12.7 µm Au UME at +0.8 V to produce $Fe(CN)_6^{3-}$. The incident $Fe(CN)_6^{3-}$ on the array is detected by ECL at +2.0 V bias voltage. As the UME is moved laterally across the array, the detected

diffusion layer precisely follows the UME movement. (b) Optical frames displaying the UME's diffusion layer movement. A full video of this process is shown in **Movie S2**.

We next aimed to determine if crosstalk (electron transfer between neighboring electrodes) was occurring since it has been reported for previous closed-bipolar array fabrication schemes.[28] Elimination of crosstalk is important to ensure single-electrode spatial resolution. We investigated this behavior by using a generator-collector setup as shown in **Figure 4a**, similar to the setup used in our previous work.[30] Here, a 12.7 µm Au UME was positioned ~100 µm above the array surface in a 50 mM $Fe(CN)_6^{4-}$ solution. A +0.8 V potential was applied to the Au UME, producing $Fe(CN)_6^{3-}$ which diffused toward the array. The diffusion layer was optically detected across the biased (+2V) bipolar array by coupling to anodic ECL.

Upon activation of the generator electrode, a 3-electrode cluster in the array was immediately illuminated by ECL. The generator electrode was then moved laterally across the array with a micro-positioner and the corresponding array illumination precisely followed its movement with no perceptible lag. **Figure 4b** displays four illuminated positions, with the full video shown in **Movie S2**. This result suggests that the relatively constant size of the diffusion layer was uniformly detected. If crosstalk were present, we would expect to observe overlap of the signal from neighboring electrodes. While it is possible for toppling of the electrodes to occur prior to Parylene deposition, these occurrences are easily observable and may be screened out during the fabrication process. Nonetheless, we verified that the arrays were absent from crosstalk by scanning the generator electrode across thousands of other array electrodes in subsequent experiments.

We next aimed to explore our capacity to map variable redox concentrations across a wide area. Here, we positioned a micropipette filled with 100 mM $Fe(CN)_6^{3-}$ 100 µm away from the array, as shown in **Figure 5a**. A pressure-injection module was used to dispense the $Fe(CN)_6^{3-}$ at pressures between 0.5 and 2 PSI and durations from 1 to 10 s. Reduction of $Fe(CN)_6^{3-}$ was coupled to anodic ECL across the bipolar array electrodes which were driven by a +2.8 V bias voltage.

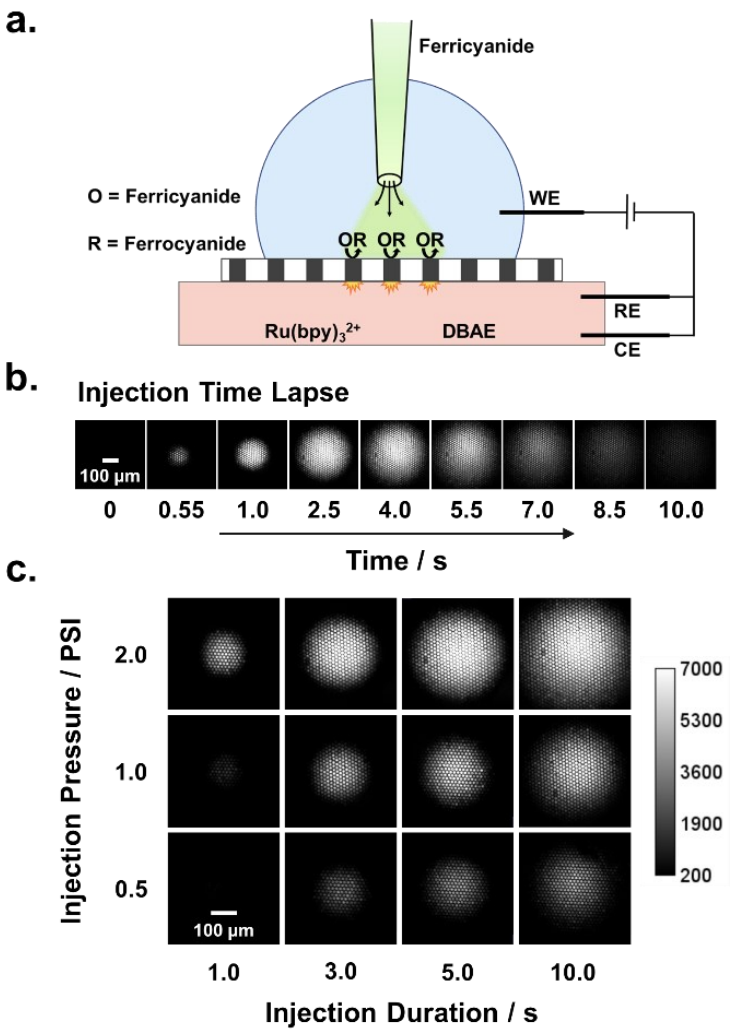

Figure 5. (a) Schematic displaying the injection of $Fe(CN)_6^{3-}$ from a micropipette onto the array. $Fe(CN)_6^{3-}$ was detected by coupling to anodic ECL across the biased bipolar array (+2.0 V). (b) Time-lapse images of a single injection using 2 PSI for 5 s. The variable ECL intensities are due to the detected heterogeneity in $Fe(CN)_6^{3-}$ concentration. A full video of this injection is shown in **Movie S3**. (c) Maximum intensity frames collected during 12 independent injection experiments using the described injection pressure and duration conditions. The calibration bar to the right of (c) describes the ECL intensity for (b) and (c).

In **Figure 5b** we show an example $Fe(CN)_6^{3-}$ injection time lapse using 2 PSI for 5 s. Variations in ECL intensity and illuminated regions are observed depending on the time point during the injection. The illumination zone begins as a ~150 µm diameter cluster at 0.09 s and grows in area until the pressure is turned off at 5 s, resulting in a zone diameter of ~1 mm. After the pressure is turned off, the intensity gradually fades due to decreased $Fe(CN)_6^{3-}$ convection paired with dilution by the bulk KCl solution.

Under constant potential, the I_{ECL} fluctuations must be due to local changes in $Fe(CN)_6^{3-}$ concentration. In **Figure 5b** we observe higher $Fe(CN)_6^{3-}$ concentrations near the center of the plume during the injection period which implies a faster convective flow velocity. This is in good agreement with simulations of convective flow profiles from a micropipette by Unwin and co-workers.[47-49]

Figure 5c compares the maximum intensities from 12 puffing experiments using the annotated injection pressure and duration conditions. We observe that a high pressure and short duration (2 PSI, 0.5 sec) more effectively delivers $Fe(CN)_6^{3-}$ to the array compared to a low pressure over a long duration (0.5 PSI, 10 sec). This effect can be attributed to increased convective mass transfer at higher pressures, thereby displacing more KCl solution from the array surface.[48] Overall, these results demonstrate that we can map changing redox concentrations during dynamic time-resolved redox processes.

We lastly examined the time-resolved formation of a redox depletion zone from a generator-collector setup in a confined space. The experiment used a setup similar to the one shown in **Figure 4**. A major difference was the use of a larger 50 µm Au UME with a 2 mm glass sheath held at a fixed position ~100 µm above the array. An oxidizing potential of +0.8 V was applied to the Au UME to generate $Fe(CN)_6^{3-}$ via $Fe(CN)_6^{4-}$ oxidation which then diffused to the array surface. The diffusion layer was optically probed on the bipolar array by coupling $Fe(CN)_6^{3-}$ reduction to the anodic ECL.

Interestingly, we observed a starkly different behavior than in **Figure 4**. A larger illumination zone was immediately detected which was indicative of the larger diffusion layer about the 50 µm Au UME. This illuminated area grew to ~400 µm over the first 2 s, with greater ECL intensity being observed near the center than at the edges. However, beginning at 3 s, the center of the illumination began to steadily decrease in intensity until a dark depletion zone was formed directly beneath the Au UME position. Over time, both the illumination and depletion regions pushed further outward away from the original Au UME location.

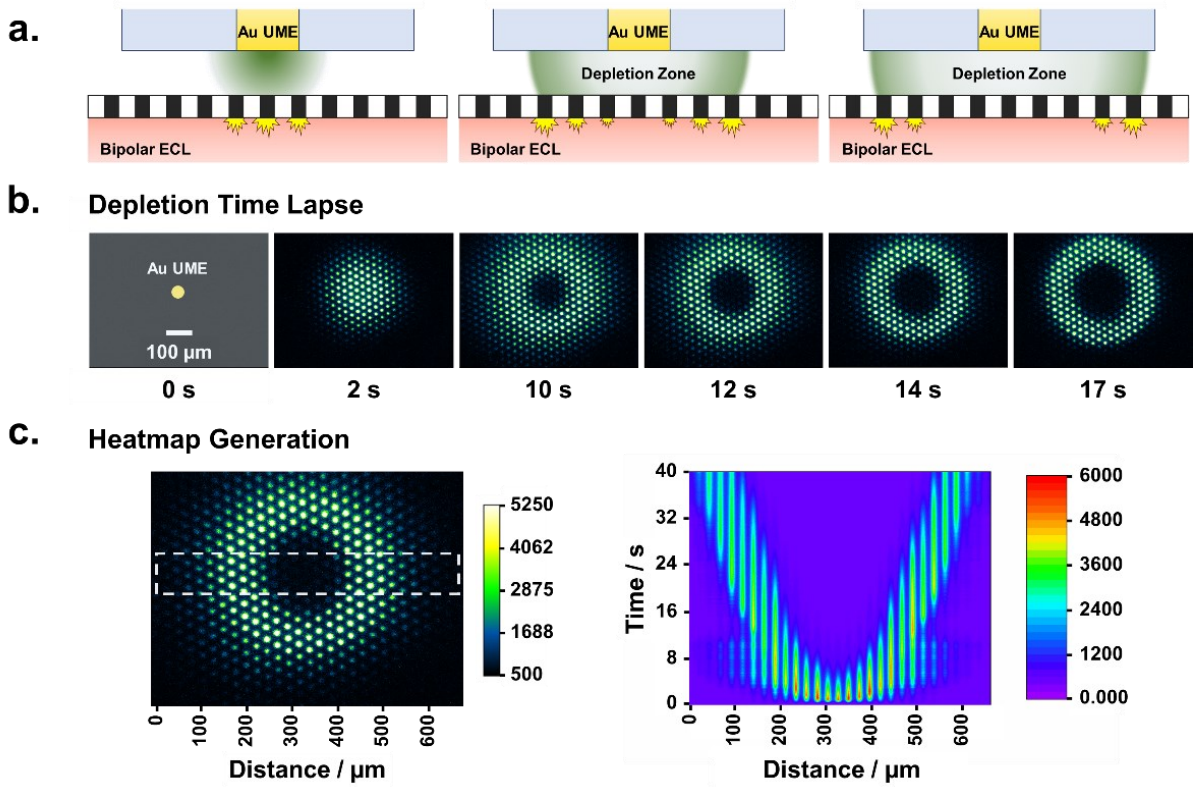

Figure 6. (a) Schematic showing the formation of a depletion zone in a generator-collector setup. $Fe(CN)_6^{4-}$ is oxidized on a 50 µm Au UME generating $Fe(CN)_6^{3-}$. The incident $Fe(CN)_6^{3-}$ on the biased array (+2.0 V) is visually detected by anodic ECL. A dark redox depletion zone is formed due to the consumption of $Fe(CN)_6^{4-}$ in the ~100 µm micro-gap between the UME and array. **(b)** Progression of the ECL response during the depletion time lapse. **(c)** Heatmap generated using the section of the array enclosed in the dotted white box on the left. The result on the right shows the average intensity at each distance within the selected region for the duration of the video. The calibration bars on the left and right of the heatmap are both in units of I_{ECL}. The full video of this process can be viewed in **Movie S4**.

We believe the formation of the depletion zone is due to a multi-step interaction between the mass transfer at the Au UME and array electrodes, as illustrated in **Figure 6a**. An initial oxidation of 50 mM $Fe(CN)_6^{4-}$ near the Au UME generates $Fe(CN)_6^{3-}$ which diffuses radially outward. Hindered diffusion due to confinement in the ~100 µm micro-gap steadily decreases the available $Fe(CN)_6^{4-}$ at the UME surface. While $Fe(CN)_6^{4-}$ may continue to diffuse to the UME from the sides, the center region directly beneath the UME can no longer receive $Fe(CN)_6^{4-}$. Therefore, less and less $Fe(CN)_6^{3-}$ could be generated

from this region leading to the formation of the observed depletion zone, which is shown in panels 2-6 in **Figure 6b**.

In **Figure 6c** we support this mechanism by creating a heatmap that illustrates how the ECL intensity of the selected area changes over the recording duration. Importantly, the heatmap indicates that both the diffusion layer and depletion zones grow radially outward at the same rate as evidenced by the steady thickness of the I_{ECL} ring. This observation suggests that both regions are controlled by the same diffusion-limited mass transfer process and are likely emanating from the same UME point source. Consequently, we expect the size of the depletion zone to be directly influenced by the diameter of the generating UME. Overall, these results demonstrate the excellent electrochemical imaging capacity of our bipolar array for dynamic time-resolved processes.

Conclusions. In summary, we have successfully fabricated uniform, massive arrays of carbon bipolar UMEs using a reproducible microfabrication procedure. This process uses carbon pyrolysis and Parylene deposition to yield an ultrathin freestanding Parylene film containing >140,000 highly uniform bipolar carbon UMEs. These arrays have been used to study several dynamic processes, including tracing the motion of an Au UME, imaging the pressure-driven flow of redox species from a micropipette, and characterizing the generation, diffusion, and depletion of $Fe(CN)_6^{3-}$ on an Au UME. The spatial resolution was found to be limited by the size of the bipolar UMEs and their spacing, which can be further improved by reducing the electrode dimensions and the interelectrode spacing. The temporal resolution, on the other hand, is limited only by the data transfer rate of the camera. Our results have further confirmed that microfabricated UME arrays are uniquely suited to imaging fast and dynamic redox processes. Future work will focus on developing this bipolar imaging system to create a massively parallelized screening platform for efficient elucidation of the performance of metal electrocatalysts.

Acknowledgements. This research was supported by the National Science Foundation (CHE-1904426). Part of this work was also conducted at the Washington Nanofabrication Facility / Molecular Analysis Facility, a National Nanotechnology Coordinated Infrastructure (NNCI) site at the University of Washington, which is supported in part by funds from the National Science Foundation (awards NNCI-1542101, 1337840 and 0335765), the National Institutes of Health, the Molecular Engineering & Sciences Institute, the Clean Energy Institute, the Washington Research Foundation, the M. J. Murdock Charitable Trust, Altatech, ClassOne Technology, GCE Market, Google and SPTS.

Associated Content. *Supporting Information.* Supporting videos of ECL-CV, generator-collector electrode experiments, $Fe(CN)_6^{3-}$ redox concentration mapping, and depletion zone imaging in addition to analysis of homogeneity of ECL intensity during ECL-CV and chemicals/materials. This information is available free of charge on the ACS Publications website.

Notes. The authors declare no competing financial interest.

References

(1) Lin, T.-E.; Rapino, S.; Girault, H. H.; Lesch, A. "Electrochemical Imaging of Cells and Tissues." *Chem. Sci.* **2018**, *9*, 4546–4554.
(2) Conzuelo, F.; Schulte, A.; Schuhmann, W. "Biological Imaging with Scanning Electrochemical Microscopy." *Proc. R. Soc. A* **2018**, *474*, 20180409.
(3) Takahashi, Y.; Kobayashi, Y.; Wang, Z.; Ito, Y.; Ota, M.; Ida, H.; Kumatani, A.; Miyazawa, K.; Fujita, T.; Shiku, H.; Korchev, Y. E.; Miyata, Y.; Fukuma, T.; Chen, M.; Matsue, T. "High-Resolution Electrochemical Mapping of the Hydrogen Evolution Reaction on Transition-Metal Dichalcogenide Nanosheets." *Angew. Chem. Int. Ed.* **2020,** *59*, 3601–3608.
(4) Zhu, M.-J.; Pan, J.-B.; Wu, Z.-Q.; Gao, X.-Y.; Zhao, W.; Xia, X.-H.; Xu, J.-J.; Chen, H.-Y. "Electrogenerated Chemiluminescence Imaging of Electrocatalysis at a Single Au-Pt Janus Nanoparticle." *Angew. Chem. Int. Ed.* **2018**, *57*, 4010–4014.
(5) Zou, N.; Chen, G.; Mao, X.; Shen, H.; Choudhary, E.; Zhou, X.; Chen, P. "Imaging Catalytic Hotspots on Single Plasmonic Nanostructures via Correlated Super-Resolution and Electron Microscopy." *ACS Nano* **2018**, *12*, 5570–5579.
(6) Amemiya, S.; Bard, A. J.; Fan, F.-R. F.; Mirkin, M. V.; Unwin, P. R. "Scanning Electrochemical Microscopy." *Ann. Rev. Anal. Chem.* **2008**, *1*, 95–131.
(7) Ebejer, N.; Schnippering, M.; Colburn, A. W.; Edwards, M. A.; Unwin, P. R. "Localized High Resolution Electrochemistry and Multifunctional Imaging: Scanning Electrochemical Cell Microscopy." *Anal. Chem.* **2010**, *82*, 9141–9145.
(8) Chen, C.-C.; Zhou, Y.; Baker, L. A. "Scanning Ion Conductance Microscopy." *Ann. Rev. Anal. Chem.* **2012**, *5*, 207–228.
(9) Takahashi, Y.; Kumatani, A.; Shiku, H.; Matsue, T. "Scanning Probe Microscopy for Nanoscale Electrochemical Imaging." *Anal. Chem.* **2017**, *89*, 342–357.

(10) Hao, R.; Peng, Z.; Zhang, B. "Single-Molecule Fluorescence Microscopy for Probing the Electrochemical Interface." *ACS Omega* **2020**, *5*, 89–97.
(11) Fan, Y.; Anderson, T. J.; Zhang, B. "Single-Molecule Electrochemistry: From Redox Cycling to Single Redox Events." *Curr. Opin. in Electrochem.* **2018**, *7*, 81–86.
(12) Chen, Y.; Zhao, D.; Fu, J.; Gou, X.; Jiang, D.; Dong, H.; Zhu, J.-J. "In Situ Imaging Facet-Induced Spatial Heterogeneity of Electrocatalytic Reaction Activity at the Subparticle Level via Electrochemiluminescence Microscopy." *Anal. Chem.* **2019**, *91*, 6829-6835.
(13) Sambur, J. B.; Chen, T.-Y.; Choudhary, E.; Chen, G.; Nissen, E. J.; Thomas, E. M.; Zou, N.; Chen, P. "Sub-Particle Reaction and Photocurrent Mapping to Optimize Catalyst-Modified Photoanodes" *Nature* **2016**, *530*, 77–80.
(14) Sambur, J. B.; Chen, P. "Distinguishing direct and indirect photoelectrocatalytic oxidation mechanisms using quantitative single-molecule reaction imaging and photocurrent measurements." *J. Phys. Chem. C* **2016**, *120*, 20668–20676.
(15) Zhang, J.; Zhou, J.; Tian, C.; Yang, S.; Jiang, D.; Zhang, X.-X.; Chen, H.-Y. "Localized Electrochemiluminescence from Nanoneedle Electrodes for Very-High-Density Electrochemical Sensing." *Anal. Chem.* **2017**, *89*, 11399–11404.
(16) Cui, C.; Jin, R.; Jiang, D.; Zhang, J.; Zhu, J.-J. "Electrogenerated Chemiluminescence in Submicrometer Wells for Very High-Density Biosensing." *Anal. Chem.* **2020**, *92*, 578–582.
(17) Yang, M.; Batchelor-McAuley, C.; Kätelhön, E.; Compton, R. G. "Reaction Layer Imaging Using Fluorescence Electrochemical Microscopy." *Anal. Chem.* **2017**, *89*, 6870–6877.
(18) Pruchyathamkorn, J.; Yang, M.; Amin, H. M. A.; Batchelor-McAuley, C.; Compton, R. G. "Imaging Electrode Heterogeneity Using Chemically Confined Fluorescence Electrochemical Microscopy." *J. Phys. Chem. Lett.* **2017**, *8*, 6124–6127.
(19) Fuladpanjeh-Hojaghan, B.; Elsutohy, M. M.; Kabanov, V.; Heyne, B.; Trifkovic, M.; Roberts, E. P. L. "In-Operando Mapping of pH Distribution in Electrochemical Processes." *Angew. Chem.* **2019**, *131*, 16971–16975.
(20) Mao, X.; Liu, C.; Hesari, M.; Zou, N.; Chen, P. "Super-Resolution Imaging of Non-Fluorescent Reactions via Competition." *Nat. Chem.* **2019**, *11*, 687–694.
(21) Arora, A.; Eijkel, J. C. T.; Morf, W. E.; Manz, A. "A Wireless Electrochemiluminescence Detector Applied to Direct and Indirect Detection for Electrophoresis on a Microfabricated Glass Device." *Anal. Chem.* **2001**, *73*, 3282–3288.
(22) Zhan, W.; Alvarez, J.; Crooks, R. M. "Electrochemical Sensing in Microfluidic Systems Using Electrogenerated Chemiluminescence as a Photonic Reporter of Redox Reactions." *J. Am. Chem. Soc.* **2002**, *124*, 13265–13270.
(23) Mavré, F.; Chow, K.-F.; Sheridan, E.; Chang, B.-Y.; Crooks, J. A.; Crooks, R. M. "A Theoretical and Experimental Framework for Understanding Electrogenerated Chemiluminescence (ECL) Emission at Bipolar Electrodes." *Anal. Chem.* **2009**, *81*, 6218–6225.
(24) Chow, K.-F.; Mavré, F.; Crooks, R. M. "Wireless Electrochemical DNA Microarray Sensor." *J. Am. Chem. Soc.* **2008**, *130*, 7544–7545.
(25) Chow, K.-F.; Mavré, F.; Crooks, J. A.; Chang, B.-Y.; Crooks, R. M. "A Large-Scale, Wireless Electrochemical Bipolar Electrode Microarray." *J. Am. Chem. Soc.* **2009**, *131*, 8364–8365.
(26) Cox, J. T.; Guerrette, J. P.; Zhang, B. "Steady-State Voltammetry of a Microelectrode in a Closed Bipolar Cell" *Anal. Chem.* **2012**, *84,* 8797-8804.
(27) Guerrette, J. P.; Oja, S. M.; Zhang, B. "Coupled Electrochemical Reactions at Bipolar Microelectrodes and Nanoelectrodes." *Anal. Chem.* **2012***, 84*, 1609-1616.
(28) Guerrette, J. P.; Percival, S. J.; Zhang, B. "Fluorescence Coupling for Direct Imaging of Electrocatalytic Heterogeneity." *J. Am. Chem. Soc.* **2013**, *135*, 855–861.
(29) Oja, S. M.; Guerrette, J. P.; David, M. R.; Zhang, B. "Fluorescence-Enabled Electrochemical Microscopy with Dihydroresorufin as a Fluorogenic Indicator." *Anal. Chem.* **2014**, *86*, 6040–6048.
(30) Oja, S. M.; Zhang, B. "Imaging Transient Formation of Diffusion Layers with Fluorescence-Enabled Electrochemical Microscopy." *Anal. Chem.* **2014**, *86*, 12299–12307.

(31) Wydallis, J. B.; Feeny, R. M.; Wilson, W.; Kern, T.; Chen, T.; Tobet, S.; Reynolds, M. M.; Henry, C. S. "Spatiotemporal Norepinephrine Mapping Using a High-Density CMOS Microelectrode Array." *Lab Chip* **2015**, *15*, 4075–4082.
(32) Dragas, J.; Viswam, V.; Shadmani, A.; Chen, Y.; Bounik, R.; Stettler, A.; Radivojevic, M.; Geissler, S.; Obien, M. E. J.; Muller, J.; Hierlemann, A. "*In Vitro* Multi-Functional Microelectrode Array Featuring 59 760 Electrodes, 2048 Electrophysiology Channels, Stimulation, Impedance Measurement, and Neurotransmitter Detection Channels." *IEEE J. Solid-State Circuits* **2017**, *52*, 1576–1590.
(33) Tedjo, W.; Nejad, J. E.; Feeny, R.; Yang, L.; Henry, C. S.; Tobet, S.; Chen, T. "Electrochemical Biosensor System Using a CMOS Microelectrode Array Provides High Spatially and Temporally Resolved Images." *Biosens. and Bioelect.* **2018**, *114*, 78–88.
(34) Viswam, V.; Bounik, R.; Shadmani, A.; Dragas, J.; Urwyler, C.; Boos, J. A.; Obien, M. E. J.; Muller, J.; Chen, Y.; Hierlemann, A. "Impedance Spectroscopy and Electrophysiological Imaging of Cells with a High-Density CMOS Microelectrode Array System." *IEEE Trans. Biomed. Circuits Syst.* **2018**, *12*, 1356–1368.
(35) Tedjo, W.; Chen, T. "An Integrated Biosensor System with a High-Density Microelectrode Array for Real-Time Electrochemical Imaging." *IEEE Trans. Biomed. Circuits Syst.* **2019**, 1–1.
(36) Lin, X.; Zheng, L.; Gao, G.; Chi, Y.; Chen, G. "Electrochemiluminescence Imaging-Based High-Throughput Screening Platform for Electrocatalysts Used in Fuel Cells." *Anal. Chem.* **2012**, *84*, 7700–7707.
(37) Wu, M.-S.; Liu, Z.; Shi, H.-W.; Chen, H.-Y.; Xu, J.-J. "Visual Electrochemiluminescence Detection of Cancer Biomarkers on a Closed Bipolar Electrode Array Chip." *Anal. Chem.* **2015**, *87*, 530–537.
(38) Zhai, Q.; Zhang, X.; Han, Y.; Zhai, J.; Li, J.; Wang, E. "A Nanoscale Multichannel Closed Bipolar Electrode Array for Electrochemiluminescence Sensing Platform." *Anal. Chem.* **2016**, *88*, 945–951.
(39) Ino, K.; Yaegaki, R.; Hiramoto, K.; Nashimoto, Y.; Shiku, H. "Closed Bipolar Electrode Array for On-Chip Analysis of Cellular Respiration by Cell Aggregates." *ACS Sens.* **2020**, 5, 740-745.
(40) Iwama, T.; Inoue, K. Y.; Abe, H.; Matsue, T. "Chemical Imaging Using a Closed Bipolar Electrode Array." *Chem. Lett.* **2018**, *47*, 843–845.
(41) Defnet, P. A.; Zhang, B. "Detection of Transient Nanoparticle Collision Events Using Electrochemiluminescence on a Closed Bipolar Microelectrode." *ChemElectroChem* **2020**, *7*, 252–259.
(42) Defnet, P. A.; Han, C.; Zhang, B. "Temporally-Resolved Ultrafast Hydrogen Adsorption and Evolution on Single Platinum Nanoparticles." *Anal. Chem.* **2019**, *91*, 4023–4030.
(43) Wang, C.; Jia, G.; Taherabadi, L. H.; Madou, M. J. "A Novel Method for the Fabrication of High-Aspect Ratio C-MEMS Structures." *J. Microelectromech. Sys.* **2005**, *14*, 348–358.
(44) Li, W.; Rodger, D. C.; Meng, E.; Weiland, J. D.; Humayun, M. S.; Tai, Y.-C. "Wafer-Level Parylene Packaging with Integrated RF Electronics for Wireless Retinal Prostheses." *J. Microelectromech. Sys.* **2010**, *19*, 735–742.
(45) Jung, Y. H.; Qiu, Y.; Lee, S.; Shih, T.-Y.; Xu, Y.; Xu, R.; Lee, J.; Schendel, A. A.; Lin, W.; Williams, J. C.; Behdad, N.; Ma, Z. "A Compact Parylene-Coated WLAN Flexible Antenna for Implantable Electronics." *IEEE Antennas and Wireless Prop. Lett.* **2016**, *15*, 1382–1385.
(46) Trantidou, T.; Tariq, M.; Terracciano, C.; Toumazou, C.; Prodromakis, T. "The Effects of Annealing on Mechanical, Chemical, and Physical Properties and Structural Stability of Parylene C." *Sensors* **2014**, *14*, 11629–11639.
(47) Macpherson, J. V; Simjee, N.; Unwin, P. R. "Hydrodynamic Ultramicroelectrodes: Kinetic and Analytical Applications." *Electrochim. Acta* **2001**, *47*, 29–45.
(48) Bitziou, E.; Rudd, N. C.; Edwards, M. A.; Unwin, P. R. "Visualization and Modeling of the Hydrodynamics of an Impinging Microjet." *Anal. Chem.* **2006**, *78*, 1435–1443.
(49) Macpherson, J. V; Beeston, M. A.; Unwin, P. R. "Imaging Local Mass-Transfer Rates within an Impinging Jet and Studies of Fast Heterogeneous Electron-Transfer Kinetics Using the Microjet Electrode." *J. Chem. Soc. Faraday Trans.* **1995**, *91*, 899–904.

For Table of Contents Only